Open Access

Research Article

Precis. Nanomed. 2022, 5(4):963-976

Size-dependent Lattice Contraction and Oxidation State Ratio in Nano-MnO: Potential Tunable Biomedical Applications

Michael M. Ramsdell[1]*, Jenna M. Pike[2], Syed Khalid[3], & Siu-Wai Chan[1]

[1]*Columbia University, Department of Applied Physics and Applied Mathematics, New York, New York 10027*

[2]*OxEon Energy, LLC, North Salt Lake, Utah 84054*

[3]*National Synchrotron Light Source II, Brookhaven National Laboratory, Upton, New York 11973*

Submitted: August 27, 2022 Accepted: November 27, 2022 Published: November 28, 2022

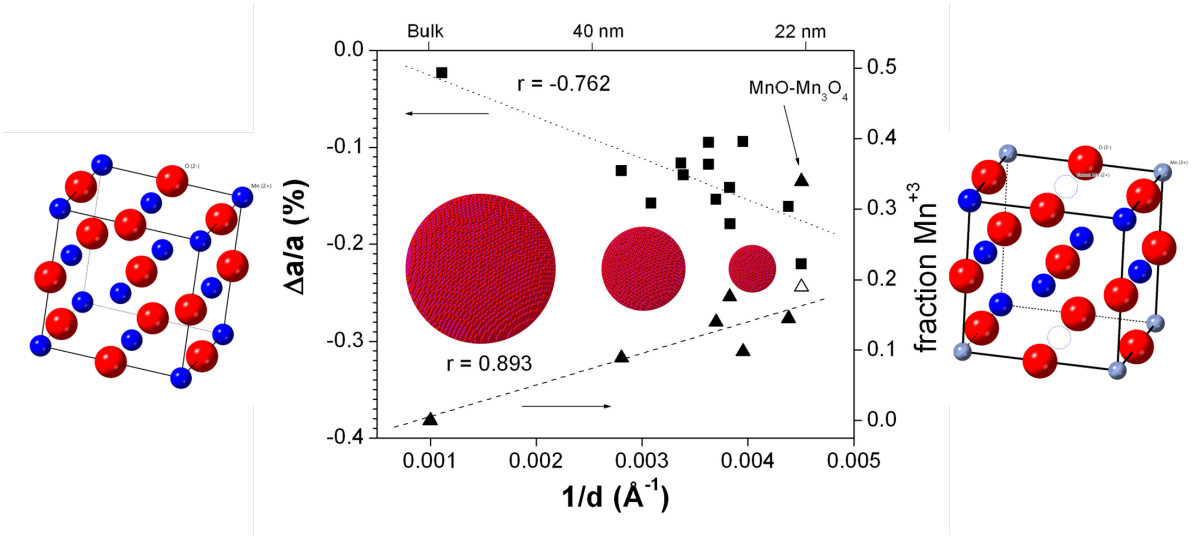

Abstract

Manganosite (MnO) nanocrystals ranging from 22 to 36 nm have been prepared by reducing hausmannite (Mn_3O_4) nanocrystals with hexamethylenetetramine ($C_6H_{12}N_4$) in a heated, H_2/N_2 gaseous environment. X-ray diffraction analysis indicates that the lattice parameter decreases by up to 0.18% (4.4379 Å) as the crystalline diameter decreases to 23 nm. X-ray absorption near edge spectroscopy demonstrates an increasing Mn^{3+} fraction from 8.9% for 36 nm diameter crystallites to 14.5% for 23 nm diameter crystallites. Thus, the lattice contraction could be partly due to the decrease of the relative cation radii from Mn^{2+} to Mn^{3+}. Yet, straight calculations of lattice parameters from the Mn^{3+} concentrations yield a 10× larger lattice contraction. We suspect the magnetic properties of the nano-MnO play a role since most oxides show a lattice expansion due to surface adsorbents. Though it is expected that the band gap should increase with decreasing size, the increasing concentration of Mn^{3+} would result in states inside the bandgap, potentially giving the appearance of a smaller bandgap. Further, the increased concentration of Mn^{3+} has potential antioxidant properties due to the dual oxidation state observed in nanocrystals of Mn_3O_4 and CeO_2 in other studies.

Rationale and Purpose

The size-dependent *lattice parameter* of nano-oxide-crystals is seldom mentioned for nano-oxides, and usually, only the lattice expansion is observed. However, in the case of nano-MnO, lattice *contraction* is observed, which has only previously been reported in α-Fe2O3 and NiO nano-oxides. Additionally, the ratio of oxidation states in nano-MnO is size dependent as well, which has potential antioxidant applications.

* Corresponding author: ramsdell.michael1@gmail.com

Introduction

Nanoscale materials continue to dominate the research sphere as much remains to be learned regarding their properties and how they vary from the bulk-crystalline form. Ceramic nanocrystals, especially transition metal oxides, are under continued examination due to their potential use in several applications, from electronics to environmental agents. Manganese oxide, also known as manganosite (MnO), nanocrystals, in particular, have extensive uses in varied fields, such as in supercapacitors [1], lithium-ion and zinc-ion batteries [2]–[4], catalytic abatement of volatile organic compounds and water-splitting catalysts [5]–[8], and in the biomedical field in magnetic resonance imaging and chemotherapy [9], to name a few.

One area of research that is attracting a significant amount of interest in the biomedical field is the use of MnO nanocrystals as a spin-lattice (T1) contrast agent in magnetic resonance imaging due to its improved relaxivity and low cytotoxicity compared to the current industry standard gadolinium contrasting agent [10]. Along with their MRI applications, MnO nanocrystals have promising applications in cancer treatment, specifically as a delivery mechanism for chemotherapeutic drugs and, more recently, in imaging-guided photothermal therapy to target tumor cells directly [11]–[13].

The interaction of nanoparticles in the biomedical environment at the nano-bio interface remains of significant interest, both to improve the efficacy of nano-based treatments as well as reduce toxicity [14]. This interface is governed by several properties of particular interest to MnO nanocrystals, such as valence states, crystallinity, defects, surface charge, and energy [15], [16]. Additionally, the cellular uptake of nanocrystals is impacted by nanocrystal size, shape, and surface chemistry [17], [18]. Manganese is a naturally occurring element in the human body, found in various cells and proteins. As such, MnO has the potential to be biocompatible in many different applications beyond those discussed previously [19]. By developing a deeper understanding of how these properties listed above relate to crystal shape, size, and structure, the MnO nanocrystals could be enhanced such that they are optimized for specific applications.

There have been several recent studies investigating MnO nanocrystal synthesis, such as combining manganese acetate with organic ligand surfactants [20], thermal decomposition [21]–[23], and inert gas condensation [24]. In this study, MnO nanocrystals were first formed by mixing manganese nitrate hydrate ($Mn(NO_3)_2{\cdot}xH_2O$) with hexamethylene-tetramine ($C_6H_{12}N_4$), hereafter HMT. Fujita et al. initially explored nanocrystal synthesis via HMT in the 1980s to prepare zinc oxide powders of various particle sizes and shapes larger than nanoscale [25]. The use of HMT to synthesize nanocrystalline metal oxides has been extensively explored by this group, most notably Cu_2O, CeO_2, and Mn_3O_4 [26]–[28]. As confirmed by in-situ small angle x-ray scattering of nano-ceria, HMT aids in nanocrystal synthesis via decomposition, thus increasing the concentration of hydroxyl ions in solution [29]. The HMT serves as a reducing catalyst in the $Mn(NO_3)_2{\cdot}xH_2O$ – HMT reaction by decomposing into ammonia, formaldehyde, and then hydroxyl and ammonium ions:

$$C_6H_{12}N_4 + 6H_2O \leftrightarrow 6H_2CO + 4NH_3 \quad \text{Eq.1a}$$

$$NH_3 + H_2O \leftrightarrow NH_4OH \leftrightarrow NH_4^+ + OH^- \quad \text{Eq.1b}$$

The hydroxyl and ammonium ions then react with the dissociated Mn^{3+} and Mn^{2+} to form Mn_3O_4 nanocrystals [28]. The Mn_3O_4 nanocrystals are then reduced with HMT in a heated H_2/N_2 gaseous environment.

Bulk manganosite crystals assume a rock salt structure, with cations and anions octahedrally coordinated and a lattice parameter of 4.446 Å (JCPDS: 71-1177). This structure, often described as two interpenetrating face-centered cubic lattices [30], has the space group $Fm\bar{3}m$ (O_m^5), Pearson symbol cF8, and Strukturbericht designation B1 [31]. Though manganosite nanocrystals share this structure, they do have some key differences from their bulk counterpart. For instance, bulk MnO is antiferromagnetic with type two ordering and a Néel temperature T_N of 118K, meaning that the magnetic moments of cations on the (111) planes are parallel and antiparallel between adjacent (111) planes below 118K [32]–[34]. However, multiple studies have found that when MnO nanoclusters are sufficiently small, specifically 5 to 10 nm, MnO displays a ferromagnetic weak behavior at low temperatures [35]–[37]. Electronically, bulk MnO crystals have a direct

bandgap between 3.9 ± 0.4 eV [38]. It is expected that, as nanocrystalline diameter decreases, the bandgap should increase due to quantum confinement [39]. However, multiple studies utilizing ultraviolet (UV)-visible spectroscopy have found that nanocrystals ranging from 14 nm to 45 nm have a bandgap less than or equivalent to the bulk MnO bandgap, ranging from 3.9 eV to 3.1 eV, respectively [37], [40]. Additionally, Vijayamari *et al.* found that photoluminescence spectroscopy yielded a broad, asymmetric peak at 3.30 eV and a 375 nm wavelength, potentially indicating a blue and green fluorescence emission [40]. A significant difference, from a physical perspective, between bulk and nanocrystalline MnO is their respective lattice parameter. Density functional theory first-principles calculations performed on $(MnO)_x$ clusters found that the bonding is partially ionic and that the average bond distance is insensitive to cluster size [41]. However, these clusters ranged from $(MnO)_3$ to $(MnO)_9$. This study has demonstrated that, similar to α-Fe_2O_3 and NiO nanoparticles [42], [43], as the size of MnO nanocrystals decreases, the lattice parameter contracts. Though there are recent studies on lattice parameter of nano-oxides showing lattice variation with decreasing crystal-size, there has been no similar study on nano-MnO.

Materials and Methods

Nanocrystals of Mn_3O_4 were synthesized via a standard method using manganese nitrate hydrate ($Mn(NO_3)_2{\cdot}xH_2O$) and hexamethylenetetramine ($C_6H_{12}N_4$), or HMT. A synthesis flow chart can be seen in Figure 1 below. A more detailed synthesis description can be found in the following references [28], [44]. The Mn_3O_4 nanocrystals in a ceramic boat were placed inside a mullite tube containing recrystallized HMT to aid in the reduction process. The nanocrystals were subsequently heated in a CM tube furnace to 550°C to 600°C at 400°C/hr in a controlled gaseous atmosphere, consisting of 8.6% H_2 to 91.4% N_2 with a flow rate of 100cm^3/min. The heat-treated nanocrystals were left to cool to ambient after reaching the maximum temperature.

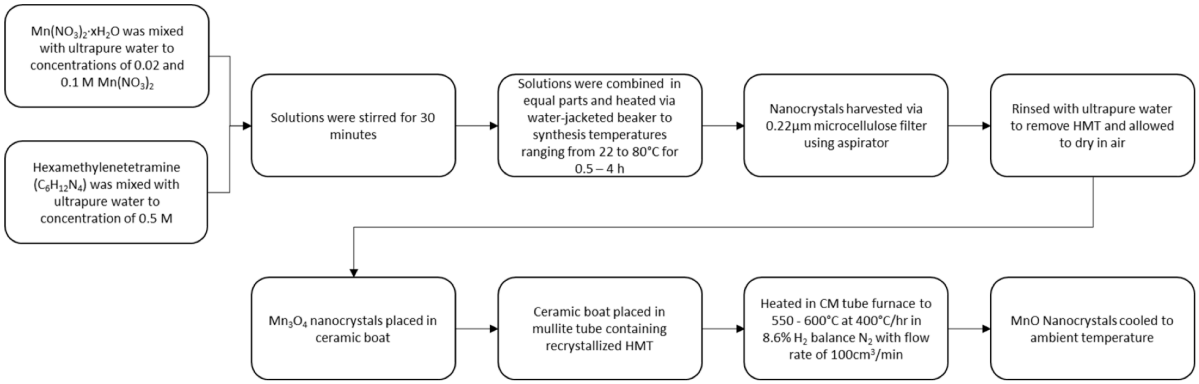

Figure 1: Synthesis flow chart starting with precursor Manganese Nitrate Hydrate ($Mn(NO_3)_2{\cdot}xH_2O$) and Hexamethylenetetramine ($C_6H_{12}N_4$).

MnO bulk and nanocrystal x-ray diffraction patterns were collected via a Scintag X_2 x-ray diffractometer, utilizing Cu-Kα radiation at a scan rate of 0.02°/step and 5s/step at ambient temperature and pressure. The diffraction patterns were then analyzed via XFIT open-source program to obtain the exact peak positions and the full width at half maximum (FWHM). From the peak positions and FWHM, the nanocrystal size D was calculated via the Scherrer equation:

$$D = \frac{K\lambda}{B\cos\theta_B} \qquad \text{Eq.2}$$

where K is a geometric constant (0.941 for spherical grain), λ is x-ray wavelength (1.54 Å), B is the broadening due to crystallite size in radians, captured as the FWHM for the corresponding peaks, and θ_B is the Bragg angle. Typically, crystallite size would be calculated for all well-defined peaks and then averaged to obtain the best approximate size of the nanocrystal. This assumes peak broadening is predominantly due to particle size effects. Another factor that can result in broader peaks is if the crystal has a non-uniform strain. To mitigate the peak broadening due to this non-uniform strain, the (111) peak was used to calculate the crystallite diameters. The Williamson-Hall equation

can be used to confirm the presence of non-uniform strain in the MnO nanocrystals.

$$\frac{\Delta d}{d} = \frac{B \cos \theta_B}{4 \sin \theta_B} \qquad \text{Eq.3}$$

In this instance, Δd is the difference in interplanar spacing caused by non-uniform strain in the crystal. Using this equation, a Williamson-Hall plot was constructed from 35° to 102° (2θ), encompassing eight x-ray diffraction (XRD) peaks, and analyzed for non-uniform strain. Lattice parameter a was calculated via the following equation:

$$a = d\,(h^2 + k^2 + l^2)^{1/2} \qquad \text{Eq.4}$$

where d is the interplanar spacing and h, k, and l refer to the Miller Indices. The lattice parameter was calculated for the eight most prominent peaks, plotted versus $\cos^2\theta/\sin\theta$, then extrapolated to the y-intercept (θ=90°) to obtain the actual lattice parameter accurate to 0.0001Å. This approach gives high accuracy in cell-dimension measurements [45].

Quantitative phase analysis of mixed-phase samples was performed via the Rietveld Refinement method [46] with EXPGUI [47] and General Structure Analysis System (GSAS) software [48]. Using the XRD patterns, the present phases were identified and then analyzed for weight fraction using the phase components' scale parameter, unit cell volume, and unit cell mass. GSAS analysis yielded chi-squared values of less than 1.5.

X-ray absorption near edge spectra (XANES) were collected of the MnO nanocrystals at the Mn K edge using National Synchrotron Light Source I beamline X19A at Brookhaven National Lab. Micron-sized powders of MnO and Mn_2O_3 (Alfa Aesar) were used as standards for Mn^{2+} and Mn^{3+}, respectively. XANES samples of these micron-size powders and nanocrystalline powders were prepared by spreading the powder on polyimide tape. The fraction of each Mn ion in the nanocrystals was calculated from the normalized spectra using ATHENA x-ray absorption spectroscopy data processing software [49]. The fraction was calculated using the linear combination feature and fitting the nanocrystal samples to the bulk samples. Bulk Mn_3O_4 has 2/3 Mn in 3+ and 1/3 Mn in 2+ oxidation states, while bulk MnO was assumed to be monovalent [50]. Raman scattering was performed in air on MnO bulk samples, and the synthesized nanocrystals via Coherent Innova 100 continuous wave argon ion laser focused to a 2 μm spot size at a wavelength of 514.5 nm in a backscattering configuration. The maximum incident power was less than 5 mW to minimize heating the samples. The spectroscopy data were collected and dispersed with a 0.6 m triple spectrometer (SPEX 1877, Triblemate) in a subtractive configuration. The resulting dispersed spectra were collected with a UV-coated Si CCD array detector (SPEX Spectrum One). The 70 to 800 cm^{-1} frequency range was calibrated via plasma lines at a resolution of approximately 2 cm^{-1}. The positions and intensities of the peaks for bulk MnO, 28 nm MnO nanocrystals, 23 nm MnO nanocrystals, and bulk Mn_3O_4 samples were determined via Lorentzian fitting, with the background being subtracted before determining peak shifts. The scattering experiments were performed both in the air and in a gaseous N_2 environment.

Results

The reduction of Mn_3O_4 to MnO altered the powder from a burnt orange color to a dark brown color, as shown in Figure 2.

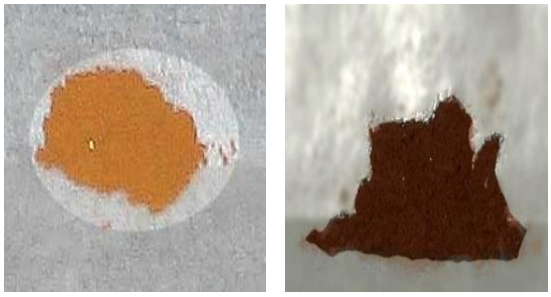

Figure 2: (Left) Mn_3O_4 nanocrystalline powder. (Right) Reduced MnO nanocrystalline powder.

The resulting brown powder was composed of nanocrystals of MnO with diameters ranging from 23 nm to 36 nm and lattice parameters varying from 4.4379 Å to 4.4395 Å, respectively. Interestingly, each batch of nano-MnO was monodisperse. These lattice parameters correspond to an approximate 0.18 to 0.15% reduction compared to the bulk parameter of 4.446 Å. The x-ray diffraction patterns obtained via a Scintag X2 XRD for the bulk MnO and nanocrystalline MnO samples are displayed in Figure 3 and Figure 4, with the former displaying the lattice planes associated with the high-intensity peaks (JCPDS: 71-1177). All samples were fully reduced to MnO except the 22 nm MnO XANES sample that contained both MnO and Mn_3O_4, as determined by XRD. The smaller nano-Mn_3O_4 were harder to be com-

pletely reduced to nano-MnO. The critical crystal-size lies just below 23nm for the present preparation procedure. As seen in Figure 4, the peaks show significant broadening compared with the bulk MnO.

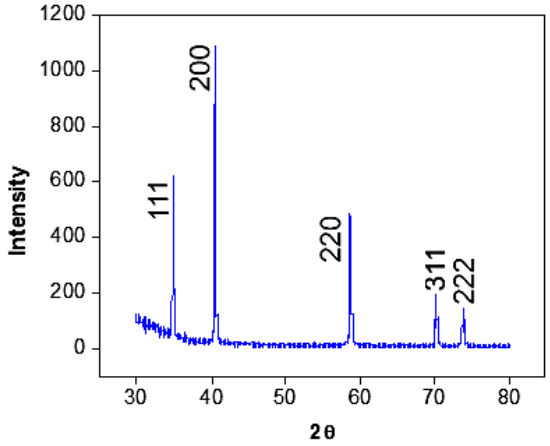

Figure 3: X-ray diffraction pattern of bulk MnO.

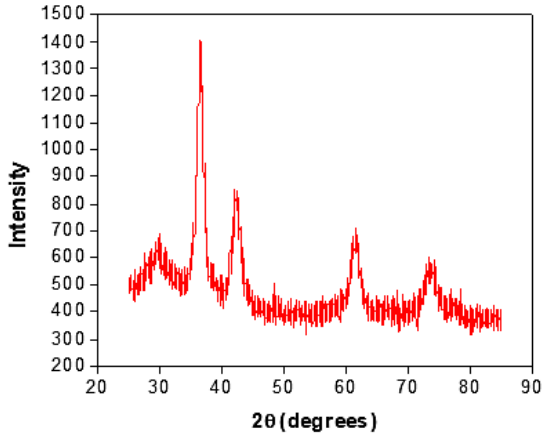

Figure 4: X-ray diffraction pattern of the 23 nm nano-MnO sample

XRD peak broadening is a commonly observed phenomenon when analyzing nanocrystals and is due to a combination of factors: the finite size of the crystal being examined and the presence of heterogeneous strain. [51].

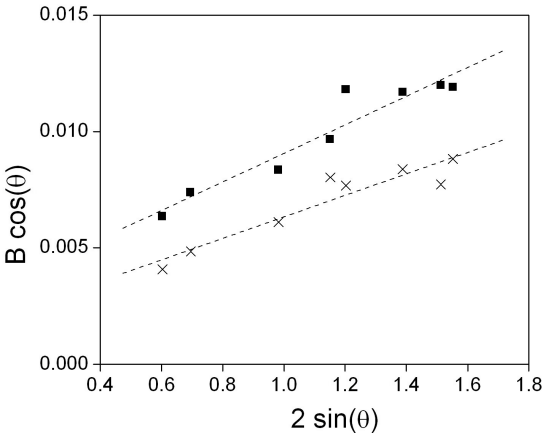

Figure 5: Williamson-Hall plot of the 23 nm (■) and 36 nm (×) crystals

The positive slope shown in the Williamson-Hall plot in Figure 5 indicates that the heterogenous, non-uniform strain present in both the 23 nm and 36 nm-MnO is larger in the 23 nm-MnO.

Therefore, the broadening of the peaks is due to the combination of nanocrystal size effects and the presence of non-uniform strain. In the case of MnO nanocrystals, the heterogeneous strain can be attributed to the non-uniform distribution of the Mn^{3+} ions and the phase change from Mn_3O_4. This phase change has a corresponding 16% decrease in unit cell volume per Mn ion [44].

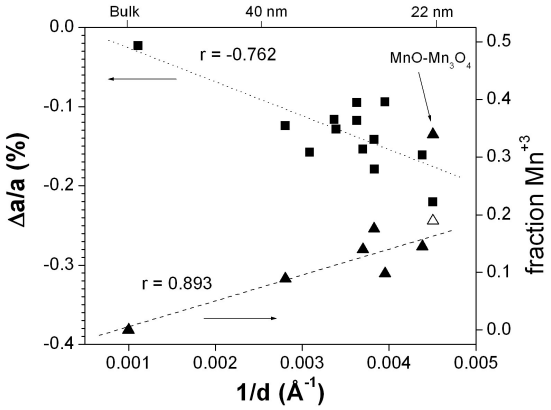

Figure 6: The left axis indicates the percent change in lattice parameter with decreasing crystallite size (■). The right axis denotes how the fraction of Mn^{3+} (◢) ions in MnO nanocrystal samples changes with crystallite size. In the mixed MnO-Mn_3O_4 sample, the Mn^{3+} fraction in the MnO phase (△) was calculated via GSAS analysis.

The percent change in the lattice parameter of MnO nanocrystals from the bulk value versus the reciprocal of the crystallite diameter can be seen in Figure 6. The negative slope indicates a lattice parameter contraction as crystallite size decreases. The dotted line is a linear fit of the data and is intended to aid in identifying the decreasing trend. The concentrations of the various oxidation states of Mn ions present in the nanocrystals were determined via XANES measurements. The resulting absorption spectra of the 22, 23, and 36 nm MnO nanocrystals were compared to the absorption spectra of bulk MnO and bulk Mn_2O_3, which were assumed to consist solely of Mn^{2+} and Mn^{3+} ions, respectively. The comparison of the nanocrystal spectra to the bulk MnO and Mn_2O_3 spectra indicated an increase in Mn^{3+} ion concentration

with a decrease in crystal size. Bulk and nanocrystalline MnO display a weak peak at 6541 eV above the threshold, followed by a steep rise to a shoulder at 6550.5 eV and a strong peak at 6554.5 eV. The weak peak corresponds to the 1s to 3d transition, the shoulder corresponds to the 1s to 4s transition, and the strong peak corresponds to the 1s to 4p transition. The Mn_2O_3 spectrum displays a similar weak peak at the threshold followed by a steep rise to a wide strong peak occurring at 6559 eV, slightly to the right of the MnO strong peak. The 6559 eV peak is indicative of the +3 valence ions in Mn_2O_3. Figure 7 displays the spectra displaced upward from one another for clarity.

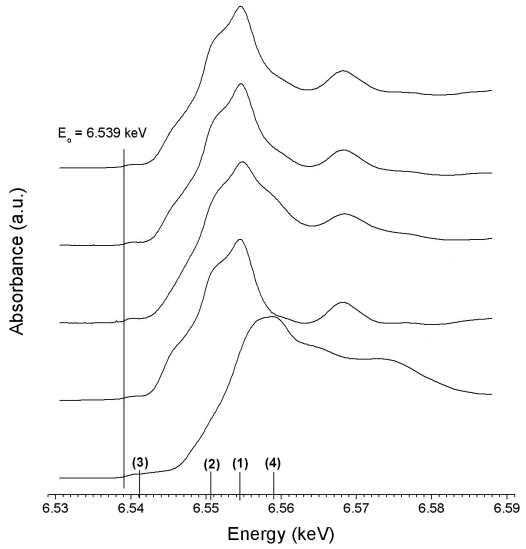

Figure 7: From top to bottom, the spectra correspond to 36 nm MnO, 23 nm MnO, 22 nm MnO (+Mn3O4), bulk MnO, and bulk Mn2O3. Labels (1) – (3) on the x-axis correspond to MnO features as follows: (1) 1s > 4p, (2) 1s > 4s, and (3) 1s > 3d transitions. The wide peak at (4) indicates Mn2O3.

The nanocrystal samples show features consistent with bulk MnO, but also display a small shoulder at 6559 eV, indicating the presence of Mn^{3+}. As shown in Figure 6, Mn^{3+} concentration increases with decreasing nanocrystal size, rising from 0% for bulk MnO to 8.9% for 36 nm and ultimately 14.5% for the 23 nm MnO nanocrystals. Further, the 22 nm mixed phase sample indicated a much higher concentration of Mn^{3+}, as expected. Using the proportions of the Mn_3O_4 and MnO phases calculated from quantitative phase analysis via the Rietveld Refinement method [46], the approximate fraction of Mn^{3+} within the MnO phase was 19%, assuming 66.7% of the Mn_3O_4 phase consisted of Mn^{3+}. Raman spectroscopy was performed on bulk Mn_3O_4, bulk MnO, 23 nm MnO nanocrystals, and 28 nm MnO nanocrystals. The expected Raman peaks for bulk MnO are at 521, 547, 595, and 645 cm^{-1}, with 521 being a broad peak and the key indicator of MnO [52]. However, recent research has shown that the key indicators of MnO are broad bands that occur at 529 and 1050 cm^{-1}, with the other wavenumbers being due to oxidation of MnO during the Raman spectroscopy process [53]. Furthermore, there is a strong correlation between oxidation states of octahedrally coordinated manganese ions, with Mn^{2+} being identified by the band around 530 cm^{-1}, Mn^{3+} having a band around 580 cm^{-1}, and Mn^{4+} with a band near 630 cm^{-1} [54]. Like Figure 7, the spectra in Figure 8 are displaced upward along the y-axis for clarity. Neither of the nanocrystalline MnO samples display a broad peak at 529 cm^{-1}.

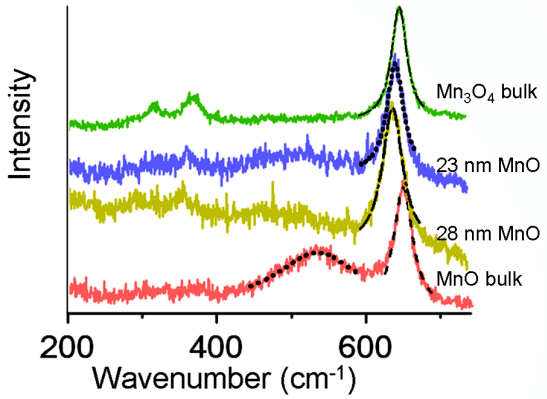

Figure 8: Raman spectra of bulk Mn3O4, 23 nm MnO, 28 nm MnO, and bulk MnO prepared from reduction of Mn_3O_4 in 8.6% H_2/91.4% N_2

Additionally, both nanocrystalline MnO samples possess a high-intensity peak at 649 cm^{-1}. Mn_3O_4 is characterized by a main band close to 658 cm^{-1}. Rusakova et al. found that MnO nanoparticles begin to oxidize to Mn_3O_4 with beam intensities as low as 0.53 mW [55]. As such, the nanocrystals of MnO had likely been partially converted back to Mn_3O_4, as evidenced by the high-intensity peaks occurring near 650 cm^{-1}. The 28 nm sample was confirmed to be a mixed phase containing MnO and Mn_3O_4, as indicated by XRD analysis.

Discussion

This study shows that, contrary to many of its fellow metal oxides, the lattice parameter of MnO nanocrystals contracts as crystallite diameter decreases [26], [56], [57]. Manganese is a transition metal with multiple oxidation states, ranging from Mn^{2+} to Mn^{7+}, as seen in

Table 1.

Table 1: Effective ionic radii of manganese cations with different oxidation states from Shannon et al. Of note, the high spin configuration is more reliable for Mn^{2+} and Mn^{3+} [58].

Ion	Effective Ionic Radii (pm)	Coordination Number
Mn^{2+}	83 (high spin), 66 (low spin)	6
Mn^{3+}	64.5 (high spin), 58 (low spin)	6
Mn^{4+}	53	6
Mn^{5+}	33	4
Mn^{6+}	25.5	4
Mn^{7+}	25	4

In bulk MnO, manganese assumes a 2+ state with an effective ionic radius of 83 pm in the high spin configuration and 66 pm in the low spin configuration [58]. As manganese becomes further oxidized, the effective ionic radius decreases to a minimum value of 25 pm, corresponding to Mn^{7+}. For comparison, the ionic radius of an octahedrally coordinated O^{2-} ion is 140 pm [58]. The estimated bulk lattice parameter (a_0) can be calculated from the O^{2-} and Mn^{2+} ionic radii via the following equation:

$$a_0 = 2(r_{O^{2-}} + r_{Mn^{2+}}) \quad \text{Eq.5a}$$

where $r_{O^{2-}}$ is the radius of an octahedrally coordinated O^{2-} ion and $r_{Mn^{2+}}$ is the ionic radius of Mn^{2+}. However, there is variation between the calculated and XRD-determined values, 4.46Å and 4.446Å, respectively. The presence of Mn with a higher oxidation state could also result in a shorter Mn – O bond. This shorter bond length, due in part to the smaller effective radius of the Mn^{3+} ion if 64.5 (high spin) and 58 pm (low spin), could contribute to the resulting lattice parameter contraction. The effect the ionic radii have on the lattice parameter can be estimated as follows:

$$a = (1 - 1.5x)a_0 + x \cdot 2(r_{O^{2-}} + r_{Mn^{3+}}) + x(1.414r_{O^{2-}}) \quad \text{Eq.5b}$$

where a is the lattice parameter, $r_{Mn^{3+}}$ is the ionic radius of Mn^{3+}, and x is the fraction of Mn^{3+}. The first parenthetical term refers to the deviation from the bulk lattice parameter. The second parenthetical term accounts for the lattice parameter change along the [100] direction due to the introduction of Mn^{3+}. The third parenthetical term is the diagonal distance from anion to anion across the oxygen octahedron with an Mn^{2+} vacancy in the center. The mechanism through which vacancies (V''_{Mn}) are introduced will be discussed (see equation 7b). As shown by the XANES measurements, the concentration of Mn^{3+} does, in fact, increase with decreasing crystal size, which suggests this is a potential factor. As such, nano-MnO is represented by $Mn_{1-x}O$ or MnO_{1+x}, depending on the defect states that accommodate the non-stoichiometry. However, the calculated percent change of the lattice parameter from equation 5b using the more reliable high spin configuration, −1.20% to −1.95%, is an order of magnitude greater than the observed percent difference of −0.15% to −0.18%. As such, there are likely other competing factors minimizing the lattice contraction.

A similar lattice parameter variation due to crystallite size-dependent ion concentration has been observed in CeO_2 and Cu_2O. In the case of CeO_2, the lattice parameter increases with decreasing size. One contributing factor to the lattice expansion is that, as the crystallite size decreases, Ce^{4+} undergoes auto-reduction to Ce^{3+}, thus increasing the concentration of Ce^{3+} and decreasing the concentration of Ce^{4+}. Specifically, 10 nm ceria particles have a 1% concentration of Ce^{3+}, and 6 nm particles have a 6%

concentration of Ce^{3+} [59], [60]. Like MnO, Song *et al*. found auto-oxidation, i.e., the concentration of Cu^{2+} increased with decreasing crystallite size in nanocrystals of Cu_2O. The lattice parameter increases with decreasing crystallite size, with 9 nm crystallites having a 0.2% larger lattice parameter than micron-size samples. However, this is attributed to the bond length of Cu (II)-O being longer than that of Cu-O [26].

A major contributing factor can be ascribed to adsorbent-induced compressive surface stress, which causes the lattice to expand. Lattice variation of small particles was first reported in the 1950s [61]. The association of surface stress to lattice parameter contraction was proposed by Dr. Kuhlmann-Wilsdorf's group in her seminal work on gold nanocrystals [62], [63]. The surface stress in this instance can be calculated, assuming the MnO nanocrystals are spherical and isotropic, by using the following equation for surface stress f_{rr}:

$$f_{rr} = -\frac{3}{4}\frac{\Delta a}{a_0}\frac{d}{K} \qquad \text{Eq.6}$$

where Δa is the change in lattice constant due to surface stress, a_0 is the bulk lattice constant, d is the crystallite diameter, and K is the compressibility. The calculated surface stress was obtained by inverting compressibility and using the experimental value for bulk modulus of 155.1 GPa [64], the results of which are shown in Table 2. The lattice parameter contraction with decreasing crystallite size yields a positive surface stress indicating the surface is in tension [65]. This calculation does assume that the bulk modulus is constant. Recent studies indicate that the bulk modulus of nano-ceria and nano-MgO are size-dependent as crystals reach the nanoscale [66], [67]. As such, further study will be required to fully understand the morphology of the nanocrystals as well as the impact on bulk modulus with decreasing size.

One potential outcome of the increased Mn^{3+} concentration is the electronic properties of MnO nanocrystals. At high temperatures and high oxygen activities, the dominant defects which occur in MnO are cation vacancies and electron holes according to the following reaction from Keller *et al*. [68], [69]:

$$\frac{1}{2}O_2 \xrightarrow{MnO} V_{Mn}^{''} + 2h^{\bullet} + O_O \qquad \text{Eq.7a}$$

Additionally, conduction in MnO is electronic, with holes dominating at high oxygen activities and electrons dominating at low oxygen activities [68], [70]. Though further studies will need to be completed to explore the dominant point defects that occur specifically in MnO nanocrystals, the following discussion explores point defect balance via Kroger-Vink notation. The increase in charge caused by higher Mn^{3+} concentration, represented by the introduction of Mn_2O_3 to the MnO nanocrystal, could equilibrate by generating cation vacancies to maintain a neutral charge balance as denoted in the following equations:

$$Mn_2O_3 \xrightarrow{MnO} 2Mn_{Mn}^{\bullet} + 3O_O^{\times} + V_{Mn}^{''} \qquad \text{Eq.7b}$$

As can be seen in equation 7b, the added positive charges from two Mn^{3+} ions are negated by creating an Mn^{2+} vacancy. Another potential mechanism by which Mn^{3+} can be incorporated into the MnO structure is via Mn^{2+} oxidation with the substitutional defect:

$$MnO \rightarrow Mn_{Mn}^{\bullet} + O_O^{\times} + e^{'} \qquad \text{Eq.7c}$$

This mechanism, however, is less likely as the calculated lattice parameter significantly decreases by 5.16 to 8.41% for the 36 and 23 nm samples, respectively, when the last term in equation 5b is ignored. The increase of cation vacancies due to the introduction of Mn^{3+} is consistent with calculations of high-temperature point defect concentrations in MnO, both pure and doped with M^{+} and M^{3+} metal ions [71].

Table 2 Surface stress of MnO nanocrystals calculated using Equation 6.

Crystallite size	Observed change of lattice parameter	Surface stress
23 nm	-0.18%	4.87 N/m
36 nm	-0.15%	6.12 N/m

The increase in Mn^{3+} concentration observed in MnO nanocrystals and potential departure from stoichiometry also has potential implications in biomedicine. CeO_2 nanocrystals, which

also demonstrate non-stoichiometry, were neuroprotective due to their direct antioxidant properties, a result of oxygen vacancies caused by the dual oxidation state present in the nanocrystals [60], [72]. Specifically, these nanocrystals were found to protect HT22 nerve cells from death due to oxidative stress [73]. However, in a later study, Lee *et al.* found that naked nano-ceria induced chemical- and size-specific changes to the neuronal cell transcriptome in mice, resulting in altered genes typically related to neurological disease, cell cycle control, and growth [74]. Hausmannite (Mn_3O_4), which also has both Mn^{2+} and Mn^{3+} present, has been shown to prevent cell damage from oxidative stress due to the Mn^{2+}/Mn^{3+} combination being an effective scavenger of reactive oxygen species, such as OH^- [75], [76] As MnO nanocrystals also appear to be nonstoichiometric with both Mn^{2+} and Mn^{3+} present, further study will be required to understand the in-vivo effects of this material.

Conclusions

This study synthesized manganosite (MnO) nanocrystals by reducing hausmannite (Mn_3O_4) nanocrystals via HMT. By examining the resulting MnO nanocrystals, it was determined that the lattice parameter contracts as the crystallite size decreases. This lattice parameter contraction could be due to multiple factors. XANES analysis showed a systematic increase in Mn^{3+} ion concentration with decreasing size. The smaller effective radius of Mn^{3+} compared to Mn^{2+} would cause a larger contraction than observed. The usual lattice expansion caused by surface adsorbents may counter the lattice contraction from the smaller Mn^{3+} cations. Nonetheless, the lattice contracts with which surface stress was calculated and found to be positive, seemingly indicating the surface is in tension. As the concentration of Mn^{3+} increases with decreasing size, the crystal becomes less stoichiometric and, as such, is more likely better represented by $Mn_{1-x}O$.

Understanding how the lattice parameter changes with nanocrystal size have significant implications, especially the associated cation oxidation. As the lattice parameter is a fundamental property of a material, the lattice parameter could be selectively tunable by controlling the size of the crystals to tailor material properties for a specific application. Lattice contraction and expansion measure the surface stress of the nanocrystals and are highly dependent on the surface species, such as surfactants or adsorbents [65]. By controlling the lattice parameter in the bio-medium of interest, certain stress states of the nanocrystals may enhance the biomedical application. Further, in the context of magnetic resonance imaging, Hyon *et al.* found that longitudinal and transversal relation time is directly related to the size of the MnO nanoparticles [77]. A deeper understanding of how the lattice parameter changes with particle size could allow for better finetuning of MnO nanocrystals as a contrast agent, although this relationship requires further exploration. To fully understand the fundamental cause and effects of the lattice contraction, further studies will be needed to determine the dominant point defect in nanocrystalline MnO as well as defect concentration, the morphology of nanocrystalline MnO via scanning electron microscope imaging and transmission electron microscopic imaging, and electrical conductivity as a function of oxygen partial pressure and lattice parameter.

Acknowledgments

This work is primarily supported by NSF DMR 1206764. Research at National Synchrotron Light Source, Center for Functional Nanomaterials, was supported by the U.S. Department of Energy, Office of Science, Office of Basic Energy Sciences, under Contract number DE-A C02-98CH10886. We would like to acknowledge Anton Dela Cruz for contributing to the study.

Conflict of interest

The authors have no relevant financial or non-financial interests to disclose. For signed statements contact the journal office editor@precisionnanomedicine.com

Refer to this article as Ramsdell MM, Pike JM, Khalid S, and Chan SW, Size-dependent Lattice Contraction and Oxidation State Ratio in Nano-MnO: Potential Tunable Biomedical Applications, *Precis. Nanomed.* 2022, 5(4):963-976, https://doi.org/10.33218/001c.56898

References

[1] H. Yuan et al., "Assembly of MnO/CNC/rGO fibers from colloidal liquid crystal for flexible supercapacitors via a continuous one-process method," Nanotechnology, vol. 30, no. 46, p. 465702, Nov. 2019, doi: 10.1088/1361-6528/ab3aaf.

[2] B. Liu, X. Hu, H. Xu, W. Luo, Y. Sun, and Y. Huang, "Encapsulation of MnO nanocrystals in electrospun carbon nanofibers as high-performance anode materials for lithium-ion batteries," Sci. Rep., vol. 4, pp. 1–6, 2014, doi: 10.1038/srep04229.

[3] T. Wang, Z. Peng, Y. Wang, J. Tang, and G. Zheng, "MnO Nanoparticle@Mesoporous Carbon composites grown on conducting substrates featuring high-performance lithium-ion battery, Supercapacitor and sensor," Sci. Rep., vol. 3, pp. 1–10, 2013, doi: 10.1038/srep02693.

[4] C. Zhu et al., "Electrochemically induced cationic defect in MnO intercalation cathode for aqueous zinc-ion battery," Energy Storage Mater., vol. 24, no. July 2019, pp. 394–401, Jan. 2020, doi: 10.1016/j.ensm.2019.07.030.

[5] K. Jin et al., "Partially oxidized sub-10 nm MnO nanocrystals with high activity for water oxidation catalysis," Sci. Rep., vol. 5, pp. 1–12, 2015, doi: 10.1038/srep10279.

[6] P. W. Menezes et al., "Nanostructured Manganese Oxides as Highly Active Water Oxidation Catalysts: A Boost from Manganese Precursor Chemistry," ChemSusChem, vol. 7, no. 8, pp. 2202–2211, Aug. 2014, doi: 10.1002/cssc.201402169.

[7] D. K. Kanan and E. A. Carter, "Band Gap Engineering of MnO via ZnO Alloying: A Potential New Visible-Light Photocatalyst," J. Phys. Chem. C, vol. 116, no. 18, pp. 9876–9887, May 2012, doi: 10.1021/jp300590d.

[8] H. Deng, S. Kang, J. Ma, L. Wang, C. Zhang, and H. He, "Role of Structural Defects in MnOx Promoted by Ag Doping in the Catalytic Combustion of Volatile Organic Compounds and Ambient Decomposition of O3," Environ. Sci. Technol., vol. 53, no. 18, pp. 10871–10879, 2019, doi: 10.1021/acs.est.9b01822.

[9] Y. Lu et al., "MnO Nanocrystals: A Platform for Integration of MRI and Genuine Autophagy Induction for Chemotherapy," Adv. Funct. Mater., vol. 23, no. 12, pp. 1534–1546, Mar. 2013, doi: 10.1002/adfm.201202233.

[10] H. Omid et al., "Synthesizing and staining manganese oxide nanoparticles for cytotoxicity and cellular uptake investigation," Biochim. Biophys. Acta - Gen. Subj., vol. 1840, no. 1, pp. 428–433, Jan. 2014, doi: 10.1016/j.bbagen.2013.10.001.

[11] M. Khalilnejad, T. Mortezazadeh, and R. G. Shayan, "Application of Manganese oxide (MnO) nanoparticles in multimodal molecular imaging and cancer therapy: A review," Nanomedicine J., vol. 8, no. 3, pp. 166–178, 2021, doi: 10.22038/NMJ.2021.57687.1598.

[12] M. Howell et al., "Manganese-loaded lipid-micellar theranostics for simultaneous drug and gene delivery to lungs," J. Control. Release, vol. 167, no. 2, pp. 210–218, Apr. 2013, doi: 10.1016/j.jconrel.2013.01.029.

[13] Y. Xiang et al., "Biocompatible and pH-sensitive MnO-loaded carbonaceous nanospheres (MnO@CNSs): A theranostic agent for magnetic resonance imaging-guided photothermal therapy," Carbon N. Y., vol. 136, pp. 113–124, Sep. 2018, doi: 10.1016/j.carbon.2018.04.058.

[14] X. He, W. G. Aker, P. P. Fu, and H.-M. Hwang, "Toxicity of engineered metal oxide nanomaterials mediated by nano–bio–eco–interactions: a review and perspective," Environ. Sci. Nano, vol. 2, no. 6, pp. 564–582, 2015, doi: 10.1039/C5EN00094G.

[15] A. E. Nel et al., "Understanding biophysicochemical interactions at the nano–bio interface," Nat. Mater., vol. 8, no. 7, pp. 543–557, Jul. 2009, doi: 10.1038/nmat2442.

[16] S. S. Atale, S. Dyawanapelly, D. D. Jagtap, R. Jain, and P. Dandekar, "Understanding the nano-bio interactions using real-time surface plasmon resonance tool," Int. J. Biol. Macromol., vol. 123, pp. 97–107, Feb. 2019, doi: 10.1016/j.ijbiomac.2018.11.039.

[17] Y. Qiu et al., "Surface chemistry and aspect ratio mediated cellular uptake of Au nanorods,"

Biomaterials, vol. 31, no. 30, pp. 7606–7619, Oct. 2010, doi: 10.1016/j.biomaterials.2010.06.051.

[18] A. Albanese, P. S. Tang, and W. C. W. Chan, "The Effect of Nanoparticle Size, Shape, and Surface Chemistry on Biological Systems," Annu. Rev. Biomed. Eng., vol. 14, no. 1, pp. 1–16, Aug. 2012, doi: 10.1146/annurev-bioeng-071811-150124.

[19] B. Parker-Esquivel et al., "Association of Poly I:C RNA and Plasmid DNA onto MnO Nanorods Mediated by PAMAM," Langmuir, vol. 28, no. 8, pp. 3860–3870, Feb. 2012, doi: 10.1021/la203998r.

[20] M. Souri, V. Hoseinpour, A. Shakeri, and N. Ghaemi, "Optimisation of green synthesis of MnO nanoparticles via utilising response surface methodology," IET Nanobiotechnology, vol. 12, no. 6, pp. 822–827, Sep. 2018, doi: 10.1049/iet-nbt.2017.0145.

[21] G. H. Lee, S. H. Huh, J. W. Jeong, B. J. Choi, S. H. Kim, and H.-C. Ri, "Anomalous Magnetic Properties of MnO Nanoclusters," J. Am. Chem. Soc., vol. 124, no. 41, pp. 12094–12095, Oct. 2002, doi: 10.1021/ja027558m.

[22] J. Lee, H. Zhu, W. Deng, and Y. Wu, "Synthesis of Cu3.8Ni/CoO and Cu3.8Ni/MnO nanoparticles for advanced lithium-ion battery anode materials," Nano Res., vol. 10, no. 3, pp. 1033–1043, Mar. 2017, doi: 10.1007/s12274-016-1363-8.

[23] N. Mironova-Ulmane et al., "Synthesis and Vibration Spectroscopy of Nano-Sized Manganese Oxides," Acta Phys. Pol. A, vol. 133, no. 4, pp. 1013–1016, Apr. 2018, doi: 10.12693/APhysPolA.133.1013.

[24] M. A. Bah, G. H. Jaffari, F. A. Khan, and S. I. Shah, "Surfaces and their effect on the magnetic properties of polycrystalline hollow γ-Mn 2 O 3 and MnO nanoparticles," Appl. Surf. Sci., vol. 375, pp. 136–143, 2016, doi: 10.1016/j.apsusc.2016.02.145.

[25] K. Fujita, K. Murata, T. Nakazawa, and I. Kayama, "Crystal shapes of zinc oxide prepared by the homogeneous precipitation method.," J. Ceram. Assoc. Japan, vol. 92, no. 1064, pp. 227–230, 1984, doi: 10.2109/jcersj1950.92.1064_227.

[26] J. Song, P. P. Rodenbough, L. Zhang, and S.-W. Chan, "Size-Dependent Crystal Properties of Nanocuprite," Int. J. Appl. Ceram. Technol., vol. 13, no. 2, pp. 389–394, Mar. 2016, doi: 10.1111/ijac.12486.

[27] F. Zhang, Q. Jin, and S.-W. Chan, "Ceria nanoparticles: Size, size distribution, and shape," J. Appl. Phys., vol. 95, no. 8, pp. 4319–4326, Apr. 2004, doi: 10.1063/1.1667251.

[28] J. Pike, J. Hanson, L. Zhang, and S.-W. Chan, "Synthesis and Redox Behavior of Nanocrystalline Hausmannite (Mn 3 O 4)," Chem. Mater., vol. 19, no. 23, pp. 5609–5616, Nov. 2007, doi: 10.1021/cm071704b.

[29] P. P. Rodenbough, J. Song, D. Walker, S. M. Clark, B. Kalkan, and S. W. Chan, "Size dependent compressibility of nano-ceria: Minimum near 33 nm," Appl. Phys. Lett., vol. 106, no. 16, 2015, doi: 10.1063/1.4918625.

[30] M. De Graef and M. E. McHenry, "Metallic structures I: simple, derivative, and superlattice structures," in Structure of Materials: An Introduction to Crystallography, Diffraction and Symmetry, Second., Cambridge, United Kingdom: Cambridge University Press, 2012, pp. 425–464.

[31] G. Burns and A. M. Glazer, "Space Group Applications," in Space Groups for Solid State Scientists, Elsevier, 2013, pp. 187–274.

[32] U. D. Wdowik and D. Legut, "Ab initio lattice dynamics of MnO," J. Phys. Condens. Matter, vol. 21, no. 27, p. 275402, Jul. 2009, doi: 10.1088/0953-8984/21/27/275402.

[33] X. Sun, E. Feng, Y. Su, K. Nemkovski, O. Petracic, and T. Brückel, "Magnetic properties and spin structure of MnO single crystal and powder," J. Phys. Conf. Ser., vol. 862, p. 012027, Jun. 2017, doi: 10.1088/1742-6596/862/1/012027.

[34] B. A. Frandsen, M. Brunelli, K. Page, Y. J. Uemura, J. B. Staunton, and S. J. L. Billinge, "Verification of Anderson Superexchange in MnO via Magnetic Pair Distribution Function Analysis

and ab initio Theory," Phys. Rev. Lett., vol. 116, no. 19, p. 197204, May 2016, doi: 10.1103/PhysRevLett.116.197204.

[35] G. H. Lee, S. H. Huh, J. W. Jeong, B. J. Choi, S. H. Kim, and H. C. Ri, "Anomalous magnetic properties of MnO nanoclusters," J. Am. Chem. Soc., vol. 124, no. 41, pp. 12094–12095, 2002, doi: 10.1021/ja027558m.

[36] W. S. Seo, H. H. Jo, K. Lee, B. Kim, S. J. Oh, and J. T. Park, "Size-Dependent Magnetic Properties of Colloidal Mn3O4 and MnO Nanoparticles," Angew. Chemie Int. Ed., vol. 43, no. 9, pp. 1115–1117, Feb. 2004, doi: 10.1002/anie.200352400.

[37] J. S. Sherin, M. Harris, D. Shiney Manoj, and J. K. Thomas, "Synthesis, characterization and magnetic studies of uniform sized manganosite nanocrystals," Mater. Today Proc., vol. 4, no. 2, pp. 4403–4411, 2017, doi: 10.1016/j.matpr.2017.04.012.

[38] J. van Elp, R. H. Potze, H. Eskes, R. Berger, and G. A. Sawatzky, "Electronic structure of MnO," Phys. Rev. B, vol. 44, no. 4, pp. 1530–1537, Jul. 1991, doi: 10.1103/PhysRevB.44.1530.

[39] L. Brus, "Electronic wave functions in semiconductor clusters: Experiment and theory," J. Phys. Chem., vol. 90, no. 12, pp. 2555–2560, 1986, doi: 10.1021/j100403a003.

[40] A. Vijayamari, K. Sadayandi, S. Sagadevan, and P. Singh, "A study of optical, surface morphological and electrical properties of manganese oxide nanoparticles," J. Mater. Sci. Mater. Electron., vol. 28, no. 3, pp. 2739–2746, Feb. 2017, doi: 10.1007/s10854-016-5853-y.

[41] S. K. Nayak and P. Jena, "Equilibrium Geometry, Stability, and Magnetic Properties of Small MnO Clusters," J. Am. Chem. Soc., vol. 121, no. 4, pp. 644–652, Feb. 1999, doi: 10.1021/ja981721p.

[42] M. Sharma, S. Murugavel, D. K. Shukla, and F. M. F. De Groot, "Reversal in the Lattice Contraction of α-Fe 2 O 3 Nanoparticles," J. Phys. Chem. C, vol. 122, no. 17, pp. 9292–9301, May 2018, doi: 10.1021/acs.jpcc.8b00550.

[43] T. Tajiri, S. Saisho, M. Mito, H. Deguchi, K. Konishi, and A. Kohno, "Size Dependence of Crystal Structure and Magnetic Properties of NiO Nanoparticles in Mesoporous Silica," J. Phys. Chem. C, vol. 119, no. 2, pp. 1194–1200, Jan. 2015, doi: 10.1021/jp5112372.

[44] J. M. Pike, "Synthesis and Redox Behaviors of Copper Oxide and Manganese Oxide Nanoparticles. Ph.D. Thesis," Columbia University, New York City, United States, 2007.

[45] B. D. Cullity and S. R. Stock, "Precise Parameter Measurements," in Elements of X-ray Diffraction, Third., Upper Saddle River, New Jersey, United States: Prentice Hall, 2001, pp. 363–383.

[46] H. M. Rietveld, "A profile refinement method for nuclear and magnetic structures," J. Appl. Crystallogr., vol. 2, no. 2, pp. 65–71, Jun. 1969, doi: 10.1107/S0021889869006558.

[47] B. H. Toby, "EXPGUI, a graphical user interface for GSAS," J. Appl. Crystallogr., vol. 34, no. 2, pp. 210–213, Apr. 2001, doi: 10.1107/S0021889801002242.

[48] A. C. Larson and R. B. V. Dreele, General Structure Analysis System (GSAS). Los Alamos National Laboratory Report LAUR 86-748, 2004.

[49] B. Ravel, "ATHENA, 0.8.050.".

[50] B. Ravel and M. Newville, "ATHENA and ARTEMIS: Interactive graphical data analysis using IFEFFIT," Phys. Scr. T, vol. T115, pp. 1007–1010, 2005, doi: 10.1238/Physica.Topical.115a01007.

[51] B. D. Cullity and S. R. Stock, "Diffraction III: Real Samples," in Elements of X-ray Diffraction, Third., Upper Saddle River, New Jersey, United States: Prentice Hall, 2001, pp. 167–183.

[52] M. Bernard, A. Hugot-Le Goff, B. V. Thi, and S. Cordoba de Torresi, "Electrochromic Reactions in Manganese Oxides: I . Raman Analysis," J. Electrochem. Soc., vol. 140, no. 11, pp. 3065–3070, 1993, doi: 10.1149/1.2220986.

[53] S. Bernardini, F. Bellatreccia, A. Casanova Municchia, G. Della Ventura, and A. Sodo, "Raman spectra of natural manganese oxides," J. Raman Spectrosc., vol. 50, no. 6, pp. 873–888, 2019,

doi: 10.1002/jrs.5583.

[54] S. Bernardini, F. Bellatreccia, G. Della Ventura, and A. Sodo, "A Reliable Method for Determining the Oxidation State of Manganese at the Microscale in Mn Oxides via Raman Spectroscopy," Geostand. Geoanalytical Res., vol. 45, no. 1, pp. 223–244, 2021, doi: 10.1111/ggr.12361.

[55] I. Rusakova et al., "Nanoparticle Shape Conservation in the Conversion of MnO Nanocrosses into Mn 3 O 4," Chem. Mater., vol. 19, no. 6, pp. 1369–1375, Mar. 2007, doi: 10.1021/cm062649u.

[56] J. E. Spanier, R. D. Robinson, F. Zhang, S.-W. Chan, and I. P. Herman, "Size-dependent properties of CeO2-y nanoparticles as studied by Raman scattering," Phys. Rev. B, vol. 64, no. 24, p. 245407, Nov. 2001, doi: 10.1103/PhysRevB.64.245407.

[57] P. P. Rodenbough et al., "Lattice Expansion in Metal Oxide Nanoparticles: MgO, Co 3 O 4 , & Fe 3 O 4," J. Am. Ceram. Soc., vol. 100, no. 1, pp. 384–392, Jan. 2017, doi: 10.1111/jace.14478.

[58] R. D. Shannon, "Revised effective ionic radii and systematic studies of interatomic distances in halides and chalcogenides," Acta Crystallogr. Sect. A, vol. 32, no. 5, pp. 751–767, Sep. 1976, doi: 10.1107/S0567739476001551.

[59] F. Zhang, P. Wang, J. Koberstein, S. Khalid, and S.-W. Chan, "Cerium oxidation state in ceria nanoparticles studied with X-ray photoelectron spectroscopy and absorption near edge spectroscopy," Surf. Sci., vol. 563, no. 1–3, pp. 74–82, Aug. 2004, doi: 10.1016/j.susc.2004.05.138.

[60] F. Zhang et al., "Cerium oxide nanoparticles: Size-selective formation and structure analysis," Appl. Phys. Lett., vol. 80, no. 1, pp. 127–129, Jan. 2002, doi: 10.1063/1.1430502.

[61] F. W. C. Boswell, "Precise determination of lattice constants by electron diffraction and variations in the lattice constants of very small crystallites," Proc. Phys. Soc. Sect. A, vol. 64, no. 5, pp. 465–476, 1951, doi: 10.1088/0370-1298/64/5/305.

[62] C. W. Mays, J. S. Vermaak, and D. Kuhlmann-Wilsdorf, "On surface stress and surface tension II. Determination of the surface stress of gold," Surf. Sci., vol. 12, no. 2, pp. 134–140, Oct. 1968, doi: 10.1016/0039-6028(68)90119-2.

[63] P. R. Couchman, W. A. Jesser, D. Kuhlmann-Wilsdorf, and J. P. Hirth, "On the concepts of surface stress and surface strain," Surf. Sci., vol. 33, no. 3, pp. 429–436, 1972, doi: 10.1016/0039-6028(72)90138-0.

[64] R. E. Pacalo and E. K. Graham, "Pressure and temperature dependence of the elastic properties of synthetic MnO," Phys. Chem. Miner., vol. 18, no. 1, pp. 441–446, Jul. 1991, doi: 10.1007/BF00199046.

[65] S.-W. Chan and W. Wang, "Surface stress of nanocrystals," Mater. Chem. Phys., vol. 273, p. 125091, Nov. 2021, doi: 10.1016/j.matchemphys.2021.125091.

[66] P. P. Rodenbough, J. Song, D. Walker, S. M. Clark, B. Kalkan, and S.-W. Chan, "Size dependent compressibility of nano-ceria: Minimum near 33 nm," Appl. Phys. Lett., vol. 106, no. 16, p. 163101, Apr. 2015, doi: 10.1063/1.4918625.

[67] P. P. Rodenbough and S.-W. Chan, "Crystallite-size dependency of the pressure and temperature response in nanoparticles of magnesia," J. Nanoparticle Res., vol. 19, no. 7, p. 241, Jul. 2017, doi: 10.1007/s11051-017-3922-7.

[68] M. Keller and R. Dieckmann, "Defect Structure and Transport Properties of Manganese Oxides: (I) The Nonstoichiometry of Manganosite (Mn1-ΔO)," Berichte der Bunsengesellschaft für Phys. Chemie, vol. 89, no. 8, pp. 883–893, Aug. 1985, doi: 10.1002/bbpc.19850890815.

[69] P. Kofstad, "Defects and diffusion in MnO," J. Phys. Chem. Solids, vol. 44, no. 9, pp. 879–889, Jan. 1983, doi: 10.1016/0022-3697(83)90126-9.

[70] N. G. Eror and J. B. Wagner, "Nonstoichiometric Disorder in Single Crystalline MnO," J. Electrochem. Soc., vol. 118, no. 10, p. 1665, 1971, doi: 10.1149/1.2407807.

[71] A. Stokłosa, "Point defects diagrams for pure and doped manganese oxide Mn 1-δO in the temperature range of 1173-1830 K," Mater. Chem. Phys., vol. 134, no. 2–3, pp. 1136–1145, 2012,

doi: 10.1016/j.matchemphys.2012.04.006.

[72] R. D. Robinson, J. E. Spanier, F. Zhang, S.-W. Chan, and I. P. Herman, “Visible thermal emission from sub-band-gap laser excited cerium dioxide particles,” J. Appl. Phys., vol. 92, no. 4, pp. 1936–1941, Aug. 2002, doi: 10.1063/1.1494130.

[73] D. Schubert, R. Dargusch, J. Raitano, and S.-W. Chan, “Cerium and yttrium oxide nanoparticles are neuroprotective,” Biochem. Biophys. Res. Commun., vol. 342, no. 1, pp. 86–91, Mar. 2006, doi: 10.1016/j.bbrc.2006.01.129.

[74] T.-L. Lee, J. M. Raitano, O. M. Rennert, S.-W. Chan, and W.-Y. Chan, “Accessing the genomic effects of naked nano-ceria in murine neuronal cells,” Nanomedicine Nanotechnology, Biol. Med., vol. 8, no. 5, pp. 599–608, Jul. 2012, doi: 10.1016/j.nano.2011.08.005.

[75] Y. Liu and J. Shi, “Antioxidative nanomaterials and biomedical applications,” Nano Today, vol. 27, pp. 146–177, Aug. 2019, doi: 10.1016/j.nantod.2019.05.008.

[76] N. Singh, M. A. Savanur, S. Srivastava, P. D’Silva, and G. Mugesh, “A manganese oxide nanozyme prevents the oxidative damage of biomolecules without affecting the endogenous antioxidant system,” Nanoscale, vol. 11, no. 9, pp. 3855–3863, 2019, doi: 10.1039/C8NR09397K.

[77] H. Bin Na et al., “Development of aT1 Contrast Agent for Magnetic Resonance Imaging Using MnO Nanoparticles,” Angew. Chemie, vol. 119, no. 28, pp. 5493–5497, Jul. 2007, doi: 10.1002/ange.200604775.